J. Fluid Mech. (2003), *vol.* 495, *pp.* 35–55. © 2003 Cambridge University Press
DOI: 10.1017/S0022112003006074 Printed in the United Kingdom

Resonant Langmuir-circulation–internal-wave interaction. Part 1. Internal wave reflection

By G. P. CHINI[1] AND S. LEIBOVICH[2]

[1]Mechanical Engineering Department, University of New Hampshire, Durham, NH 03824, USA

[2]Sibley School of Mechanical and Aerospace Engineering, Cornell University, Ithaca, NY 14853, USA

(Received 8 July 2002 and in revised form 9 June 2003)

Langmuir circulation is a convective motion commonly observed in the oceanic mixed layer. Internal waves are a prominent feature of stratified regions, particularly the thermocline bounding the mixed layer. Here, the potential for Langmuir-circulation–internal-wave coupling is investigated using a two-layer ocean model. The density jump across the sharp thermocline confines all rotational motions, including the wind-aligned Langmuir vortices, to the upper ('mixed') layer. Linear analysis indicates: (i) that thermocline compliance enhances the onset of Langmuir circulation, and (ii) that the 'vortex force' arising from the interaction of surface waves with the wind-driven shear modifies the dynamics of cross-wind propagating internal waves. Weakly nonlinear analysis reveals that resonant cross-wind propagating internal waves can be nonlinearly reflected from stationary Langmuir circulation, a dynamic reminiscent of the 'Bragg reflection' of surface waves propagating over sand bars. A key feature of the reflection mechanism is the modification of the linear internal-wave dynamics by the vortex force.

1. Introduction

Langmuir circulation is a convective motion that dominates the observed kinematics of the upper oceanic mixed layer (Smith 2001). According to the widely accepted Craik–Leibovich (hereinafter referred to as CL) theory (Craik & Leibovich 1976; Craik 1977; Leibovich 1977*b*), the counter-rotating wind-aligned Langmuir vortices arise as an instability of a wind-driven shear flow on which surface waves propagate. There is ample observational and theoretical evidence that Langmuir circulation plays a prominent role in maintaining the well-mixed character of the upper ocean, accomplishing much of the transport of heat, mass and momentum within that region (Leibovich 1983). Internal waves also play a critical role in the dynamics of the upper ocean by transmitting energy and momentum and, in regions of wave degradation, by driving local mixing. The most energetic internal waves propagate along the sharp density-gradient zone – termed the pycno- or thermocline – at the base of the mixed layer (Phillips 1977).

Although Langmuir circulation and internal-wave propagation have each been studied extensively, little is known about possible interactions between these two phenomena. Leibovich (1977*a*) examined the linear stability of inviscid stably stratified shear flows in the presence of surface waves, but coupling between Langmuir-circulation and internal-wave modes was not considered. In many theoretical and numerical investigations of Langmuir circulation, the mixed layer is assumed to be bounded below by a rigid (planar) thermocline (e.g. Cox *et al.* 1992; Cox & Leibovich

https://doi.org/10.1017/S0022112003006074 Published online by Cambridge University Press

1993; Li & Garrett 1995; Tandon & Leibovich 1995), eliminating *a priori* the possibility of internal-wave motion. Several investigators have simulated Langmuir circulation in a deep 'numerical ocean' (Lele 1985; Li & Garrett 1995, 1997; Skyllingstad & Denbo 1995; McWilliams, Sullivan & Moeng 1997), but none has isolated or studied Langmuir circulation–internal wave interactions.

Observational evidence of coexisting Langmuir circulation and internal waves is given in figure 13 of Smith (1992). A comparison of Skyllingstad & Denbo's large-eddy simulations (LES) with data collected during the Coupled Ocean–Atmosphere Response Experiment also reveals the simultaneous occurrence of internal waves (see e.g. figures 1 and 9 of Skyllingstad & Denbo 1999) and Langmuir vortices. Temperature measurements obtained by Farmer during a period of intense Langmuir circulation clearly show a correlation between thermal plumes, which impinge the mixed-layer base in downwelling zones between pairs of adjacent vortices, and temperature fluctuations in the stratified water beneath the mixed layer (Farmer, Vagle & Li 2001). These data, in particular, suggest an interaction between the mixed-layer vortices and downward-radiating internal waves. Similarly, in their LES of 'Langmuir turbulence', McWilliams *et al.* (1997) attributed downward radiation of momentum beneath the mixed layer to the interaction of the Langmuir circulation with 'the stable mean stratification by a process that is not quantitatively well understood (nor accurately calculated with typical LES grid resolution).'

Thorpe (1997) has noted that small-scale internal waves and large-scale Langmuir cells have commensurate length and time scales, i.e. $O(100)$ m wavelengths and half-hour periods or eddy-turnover times. Although restricted to linearized inviscid dynamics, his analytical investigation of a two-layer ocean model was the first study to specifically address interactions between Langmuir circulation and internal (more properly, 'interfacial') waves. Thorpe's results suggest that coupling between the waves and vortices may occur over a realistic range of the imposed wind stress, mixed-layer depth and stratification.

We follow Thorpe by investigating the dynamics of a two-layer ocean model in which the discrete stratification confines the Langmuir circulation to the upper layer (see § 2). Our objectives are three-fold. First, we study the influence of thermocline compliance on the linear stability characteristics of Langmuir circulation: in all previous stability analyses of Langmuir circulation in a viscous fluid layer of finite depth, vertical displacements of the thermocline have been suppressed (see e.g. Leibovich 1985; Leibovich, Lele & Moroz 1989; Cox *et al.* 1992; Leibovich & Tandon 1993; Gnanadesikan & Weller 1995). By using a constant upper-layer eddy viscosity to parameterize the incoherent turbulence in that region, we avoid two non-physical results of Thorpe's inviscid linear-stability analysis: (i) that Langmuir modes of all wavelengths are amplified whenever the surface-wave Stokes drift has a component in the direction of the horizontally averaged shear flow, and (ii) that the wavenumber of the fastest growing mode is infinite. These two results were shown by Leibovich (1977*a*) for an unstratified upper layer. Next, we aim to identify the physical mechanism by which the Craik–Leibovich 'vortex force' modifies the linear dynamics of cross-wind propagating internal waves. As discussed in § 3, the vortex force arises from the interaction of downwind propagating surface waves with the mean shear. While the role of the vortex force in the generation of Langmuir circulation is commonly acknowledged, its effect on internal-wave propagation – first noted by Leibovich (1977*a*) and, later, by Thorpe (1997) – does not seem to be widely appreciated. In fact, this vortex-force effect plays an important role in the weakly nonlinear interaction of cross-wind propagating internal waves with

https://doi.org/10.1017/S0022112003006074 Published online by Cambridge University Press

Langmuir circulation. Our third objective is to obtain an asymptotic description of this interaction when attention is restricted to counter-propagating waves having a wavelength twice that of the Langmuir circulation. Such waves satisfy a quadratic nonlinear resonance condition with the Langmuir circulation, and, owing to the phase-matching that occurs between the modes (Phillips 1977), interact more strongly with the Langmuir circulation than do the non-resonant components of the internal wave spectrum. Our central result is that the imposed resonant internal waves are nonlinearly reflected from the stationary Langmuir circulation, a dynamic reminiscent of the 'Bragg reflection' of surface waves propagating over sand bars (Mei 1985).

In § 2, we motivate consideration of a two-layer ocean model. The governing equations and boundary conditions are formulated in § 3. In § 4, we employ a long-wavelength approximation to obtain analytical expressions for the Langmuir circulation growth rate, the internal-wave phase speed and the nonlinear coupling coefficients in the resonant interaction equations. Our results are summarized in § 5.

2. Two-layer model

Frequently, as a result of wind-driven mixing events, the mean density of the upper ten to fifty metres of the ocean in low to moderate latitudes is very nearly uniform with depth (Phillips 1977). The density increases rapidly across the thermocline, which bounds the mixed layer from below; beneath the sharp thermocline, the water column is only weakly (stably) stratified. Numerical and observational data indicate that the density jump across the thermocline is sufficiently strong to confine much of the turbulent motion (including the Langmuir circulation) to the mixed layer (see e.g. figure 2 of McWilliams *et al.* 1997 and figure 2 of Ostrovsky *et al.* 1996). Consequently, wind-driven currents typically are much faster within the mixed layer than they are beneath the thermocline.

With these conditions in mind, we employ a two-layer ocean model to investigate the interaction of Langmuir circulation, maintained near marginal stability by the wind and surface-wave forcing, with free internal waves imposed via non-zero initial conditions. The discrete stratification confines all rotational motions – the wind-driven shear flow $\boldsymbol{U}_b(z)$, the Langmuir circulation, and the incoherent small-scale turbulence – to the mixed layer. The Stokes drift velocity, $\boldsymbol{U}_s(z) = U_s(z)\,\hat{\boldsymbol{\imath}}$, associated with the surface-wave field is aligned with the applied wind stress vector, $\boldsymbol{\tau}$. The influence of the earth's rotation is neglected, so $\boldsymbol{U}_b(z)$ is also aligned with $\boldsymbol{\tau}$. For analytical simplicity, $\boldsymbol{U}_s(z)$ is assumed to be a linear function of depth, z, vanishing at the mean position of the thermocline. Near threshold, the fastest growing Langmuir modes take the form of rolls invariant in the wind (x) direction. Here, we restrict attention solely to windward-invariant motions; hence, we focus on internal waves which propagate along the thermocline in a direction normal to the axes of the Langmuir vortices.

We model the effects of the small-scale turbulence in the mixed layer with a constant eddy viscosity (ν_e). In addition to the eddy viscosity prescription, we also phenomenologically model the vertical flux of horizontal momentum caused by continual turbulent entrainment of abyssal fluid into the mixed layer. This entrainment velocity (w_e) is very small once the mixed layer has been established: w_e is of the order of a few metres per day, under constant forcing conditions – see Phillips (1977) and McWilliams *et al.* (1997). We neglect the implied (gradual) change in the mixed-layer depth.

Finally, we model the abyss as a semi-infinite inviscid region. In the absence of entrainment, viscous transport of momentum in the lower layer would be confined to

https://doi.org/10.1017/S0022112003006074 Published online by Cambridge University Press

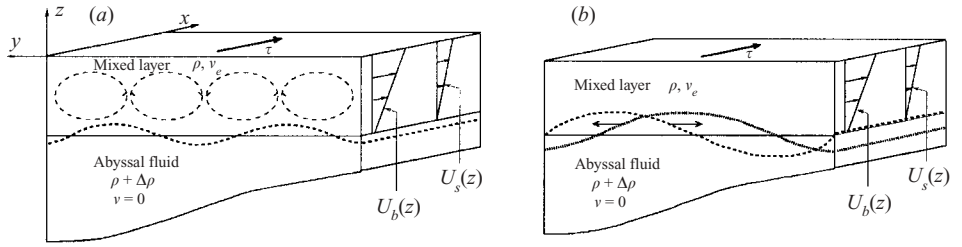


FIGURE 1. Two-layer schematic depicting (*a*) stationary Langmuir cells and (*b*) propagating internal waves. Note that the cells induce a static deformation of the thermocline.

an asymptotically thin boundary layer beneath the interface; we neglect this boundary layer in our model. Given these assumptions, the vorticity in the lower layer must remain zero for all time if it is initially zero. Thus, the lower layer is quiescent apart from inviscid irrotational disturbances driven by time-dependent interfacial displacements. Figure 1 is a schematic of the two-layer model with Langmuir-circulation and internal-wave modes separately depicted.

3. Problem formulation

As shown in figure 1, we adopt a Cartesian coordinate system in which the wind direction is aligned with the x-axis, the z-axis is vertical, with $z=0$ corresponding to the mean position of the air–sea interface, and the y-axis is directed across the wind. $\hat{\boldsymbol{\imath}}$, $\hat{\boldsymbol{\jmath}}$ and $\hat{\boldsymbol{k}}$ are unit vectors in the x-, y- and z-directions, respectively. The motion in the upper layer, which has an average depth h, is governed by the two-dimensional CL equations (Craik & Leibovich 1976; Craik 1977; Leibovich 1977*b*) with constant eddy viscosity:

$$\frac{\mathrm{D}\tilde{\boldsymbol{v}}}{\mathrm{D}\tilde{t}} = -\frac{\tilde{\boldsymbol{\nabla}}\tilde{p}}{\rho} - g\hat{\boldsymbol{k}} + \tilde{U}_s(\tilde{z})\hat{\boldsymbol{\imath}} \times (\tilde{\boldsymbol{\nabla}} \times \tilde{\boldsymbol{v}}) + \nu_e \tilde{\nabla}^2 \tilde{\boldsymbol{v}}. \tag{3.1}$$

Throughout this section, tildes are used to denote dimensional upper-layer variables. $\tilde{\boldsymbol{v}}$ is the filtered Eulerian velocity field (averaged over the 'fast' time scale associated with the period of the dominant surface waves); ρ is the constant density of the upper-layer fluid; and $\tilde{p}$ is a filtered modified pressure, referred to simply as 'pressure' unless otherwise stated. The vortex force $\tilde{U}_s(\tilde{z})\hat{\boldsymbol{\imath}} \times \left(\tilde{\boldsymbol{\nabla}} \times \tilde{\boldsymbol{v}}\right)$ accounts for the rectified effects of the surface waves. Since the lower-layer motion is assumed to be incompressible, inviscid and irrotational, the corresponding momentum equation is

$$\frac{\mathrm{D}\breve{\boldsymbol{v}}}{\mathrm{D}\breve{t}} = -\frac{\breve{\boldsymbol{\nabla}}\breve{p}}{(\rho + \Delta\rho)} - g\hat{\boldsymbol{k}}. \tag{3.2}$$

Here, as throughout, the breves denote dimensional lower-layer variables. The density in the lower layer is greater than that in the upper layer by $\Delta\rho$, with typical values of $\Delta\rho/\rho$ ranging from $O(10^{-4})$ to a maximum $O(10^{-3})$ (Phillips 1977). Since $\Delta\rho/\rho \ll 1$, internal-wave periods are much longer than those of the surface waves, so there is no contribution to the Stokes drift from the internal-wave spectrum. The internal-wave dynamics are resolved – not filtered, as for the surface waves in the CL equations.

In accord with the CL filtering operation, boundary conditions may be applied at the mean position of the air–sea interface. Because sea-surface displacements due to the internal waves are negligible (since $\Delta\rho/\rho$ is small; Phillips 1977, p. 211), this

https://doi.org/10.1017/S0022112003006074 Published online by Cambridge University Press

interface may be assumed to remain coincident with $\tilde{z}=0$, i.e. the CL-filtered vertical velocity component must vanish there:

$$\tilde{w}(\tilde{y}, 0, \tilde{t}) = 0. \tag{3.3}$$

Continuity of tangential stress across the sea surface requires

$$\nu_e \frac{\partial \tilde{\boldsymbol{v}}}{\partial z}(\tilde{y}, 0, \tilde{t}) = u_*^2 \hat{\boldsymbol{\imath}}, \tag{3.4}$$

where u_* is the water friction velocity (defined to equal $[|\boldsymbol{\tau}|/\rho]^{1/2}$). At great depth, all velocity components tend to zero:

$$\check{\boldsymbol{v}}(\check{y}, \check{z}, \check{t}) \to \boldsymbol{0} \quad \text{as} \quad \check{z} \to -\infty. \tag{3.5}$$

The motion in the upper and lower layers is related by imposing appropriate kinematic and dynamic constraints at the deformed position of the thermocline, $\tilde{z} = \check{z} = -h + \hat{\eta}$, where $\hat{\eta}$ is the (CL filtered) dimensional interfacial displacement. The kinematic constraints requiring the interface to move with the fluid are

$$\tilde{w} = \frac{\mathrm{D}\hat{\eta}}{\mathrm{D}\tilde{t}}, \quad \check{w} = \frac{\mathrm{D}\hat{\eta}}{\mathrm{D}\check{t}}. \tag{3.6}$$

The normal and tangential stress balances across the interface yield three additional conditions. In terms of the stress tensors,

$$\tilde{\Sigma}_{ij} = -\tilde{p}\delta_{ij} + \mu_e\left(\frac{\partial \tilde{v}_i}{\partial \tilde{x}_j} + \frac{\partial \tilde{v}_j}{\partial \tilde{x}_i}\right), \quad \check{\Sigma}_{ij} = -\check{p}\delta_{ij},$$

and the unit normal and tangent vectors to the interface,

$$\boldsymbol{n} = \frac{-\dfrac{\partial \eta}{\partial y}\hat{\boldsymbol{\jmath}} + \hat{\boldsymbol{k}}}{\left[1 + \left(\dfrac{\partial \eta}{\partial y}\right)^2\right]^{1/2}}, \quad \boldsymbol{t}_y = \frac{\hat{\boldsymbol{\jmath}} + \dfrac{\partial \eta}{\partial y}\hat{\boldsymbol{k}}}{\left[1 + \left(\dfrac{\partial \eta}{\partial y}\right)^2\right]^{1/2}}, \quad \boldsymbol{t}_x = \hat{\boldsymbol{\imath}},$$

where $y \equiv \tilde{y}/h \equiv \check{y}/h$ and $\eta \equiv \hat{\eta}/h$, these conditions can be written compactly as:

$$\tilde{\Sigma}_{ij} n_i n_j = \check{\Sigma}_{ij} n_i n_j, \tag{3.7}$$

$$\tilde{\Sigma}_{ij}\, t_{xi} n_j = \check{\Sigma}_{ij}\, t_{xi} n_j + w_e\left[1 + \left(\frac{\partial \eta}{\partial y}\right)^2\right]^{-1/2} \rho\,(\tilde{\boldsymbol{v}} \cdot \hat{\boldsymbol{\imath}}), \tag{3.8}$$

$$\tilde{\Sigma}_{ij}\, t_{yi} n_j = \check{\Sigma}_{ij} t_{yi} n_j + w_e\left[1 + \left(\frac{\partial \eta}{\partial y}\right)^2\right]^{-1} \times \left\{[\rho\tilde{v} - (\rho + \Delta\rho)\check{v}] + \frac{\partial \eta}{\partial y}[\rho\tilde{w} - (\rho + \Delta\rho)\check{w}]\right\}. \tag{3.9}$$

Note that (3.8) and (3.9) require discontinuities in the x- and y-directed tangential stresses across the thermocline (if present) to be balanced by the vertical flux of horizontal momentum carried by w_e, the prescribed turbulent entrainment speed. This momentum flux is non-zero whenever tangential velocity differences exist across the thermocline.

The above equations and boundary conditions admit a simple quasi-steady 'basic-state' shear flow when slow changes in the mixed-layer depth are neglected:

$$\tilde{U}_b(\tilde{z}) = u_* R_*\left(\frac{\tilde{z}}{h} + \frac{\alpha + 1}{\alpha}\right), \tag{3.10}$$

https://doi.org/10.1017/S0022112003006074 Published online by Cambridge University Press

where

$$R_* \equiv \frac{u_* h}{\nu_e}, \quad \alpha \equiv \frac{w_e h}{\nu_e}. \tag{3.11}$$

R_* is an order-unity rather than asymptotically large Reynolds number, as it is based on the eddy (rather than molecular) viscosity (Cox & Leibovich 1993). The stress-parameter α is the non-dimensional turbulent entrainment velocity across the thermocline. The basic-state pressure variation,

$$\tilde{p}_b(\tilde{z}) = \tilde{P}_b + \int_{-h}^{\tilde{z}} \rho \tilde{U}_s(\tilde{\zeta}) \frac{\mathrm{d}\tilde{U}_b}{\mathrm{d}\tilde{\zeta}}(\tilde{\zeta})\, \mathrm{d}\tilde{\zeta} - \rho g(\tilde{z} + h), \tag{3.12}$$

$$\check{p}_b(\check{z}) = \tilde{P}_b - (\rho + \Delta\rho) g(\check{z} + h), \tag{3.13}$$

where $\tilde{P}_b$ is the pressure at the thermocline, differs from a purely hydrostatic distribution by the integral term, which arises from the vertical component of the vortex force.

We are interested in the evolution of perturbations (associated with the Langmuir circulation and the internal-wave motion) to this structureless equilibrium. Hence, we decompose the velocity and pressure fields as follows:

$$\tilde{\boldsymbol{v}}(\tilde{y}, \tilde{z}, \tilde{t}) = \tilde{U}_b(\tilde{z})\hat{\boldsymbol{\imath}} + \tilde{\boldsymbol{u}}(\tilde{y}, \tilde{z}, \tilde{t}), \quad \check{\boldsymbol{v}}(\check{y}, \check{z}, \check{t}) = \check{\boldsymbol{u}}(\check{y}, \check{z}, \check{t}),$$
$$\tilde{p}(\tilde{y}, \tilde{z}, \tilde{t}) = \tilde{p}_b(\tilde{z}) + \tilde{\pi}(\tilde{y}, \tilde{z}, \tilde{t}), \quad \check{p}(\check{y}, \check{z}, \check{t}) = \check{p}_b(\check{z}) + \check{\pi}(\check{y}, \check{z}, \check{t}).$$

After scaling velocity by u_*, distance by h, time by h/u_*, and density by ρ, we obtain a set of non-dimensional equations and boundary conditions governing the evolution of perturbations to the basic state. Upper-layer perturbations satisfy the following non-dimensional equations:

$$\frac{\partial u}{\partial t} + v\frac{\partial u}{\partial y} + w\frac{\partial u}{\partial z} = -wR_* + \frac{1}{R_*}\left(\frac{\partial^2 u}{\partial y^2} + \frac{\partial^2 u}{\partial z^2}\right), \tag{3.14}$$

$$\frac{\partial v}{\partial t} + v\frac{\partial v}{\partial y} + w\frac{\partial v}{\partial z} = -\frac{\partial \pi}{\partial y} + S(1+z)\frac{\partial u}{\partial y} + \frac{1}{R_*}\left(\frac{\partial^2 v}{\partial y^2} + \frac{\partial^2 v}{\partial z^2}\right), \tag{3.15}$$

$$\frac{\partial w}{\partial t} + v\frac{\partial w}{\partial y} + w\frac{\partial w}{\partial z} = -\frac{\partial \pi}{\partial z} + S(1+z)\frac{\partial u}{\partial z} + \frac{1}{R_*}\left(\frac{\partial^2 w}{\partial y^2} + \frac{\partial^2 w}{\partial z^2}\right), \tag{3.16}$$

$$\frac{\partial v}{\partial y} + \frac{\partial w}{\partial z} = 0. \tag{3.17}$$

A velocity potential, ϕ, which satisfies the two-dimensional Laplace equation

$$\frac{\partial^2 \phi}{\partial y^2} + \frac{\partial^2 \phi}{\partial z^2} = 0, \tag{3.18}$$

where $v_l \equiv \partial\phi/\partial y$ and $w_l \equiv \partial\phi/\partial z$ are the lower-layer cross-wind velocity components, is used to describe the irrotational lower-layer motion. The non-dimensional free-surface and large-depth boundary conditions are given by

$$\frac{\partial u}{\partial z}(y, 0, t) = \frac{\partial v}{\partial z}(y, 0, t) = w(y, 0, t) = 0, \tag{3.19}$$

and

$$\phi(y, z, t) \to 0 \quad \text{as } z \to -\infty, \tag{3.20}$$

https://doi.org/10.1017/S0022112003006074 Published online by Cambridge University Press

respectively, while the interfacial conditions (evaluated at $z=-1+\eta$) are:

$$w = \frac{\partial \eta}{\partial t} + v\frac{\partial \eta}{\partial y}, \tag{3.21}$$

$$\frac{\partial \phi}{\partial z} = \frac{\partial \eta}{\partial t} + \frac{\partial \phi}{\partial y}\frac{\partial \eta}{\partial y}, \tag{3.22}$$

$$\begin{aligned} -(1+\gamma)\frac{\partial \phi}{\partial t} - \frac{(1+\gamma)}{2}|\nabla\phi|^2 = \pi + \gamma F\eta + \int_{-1}^{-1+\eta} S(1+z)\frac{\mathrm{d}\,U_b(z)}{\mathrm{d}z}\,\mathrm{d}z \\ + \left[1+\left(\frac{\partial \eta}{\partial y}\right)^2\right]^{-1}\frac{2}{R_*}\left[-\frac{\partial w}{\partial z} + \frac{\partial \eta}{\partial y}\left(\frac{\partial v}{\partial z}+\frac{\partial w}{\partial y}\right) - \left(\frac{\partial \eta}{\partial y}\right)^2\frac{\partial v}{\partial y}\right], \end{aligned} \tag{3.23}$$

$$\frac{\partial u}{\partial z} + \frac{\mathrm{d}U_b}{\mathrm{d}z} - \frac{\partial \eta}{\partial y}\frac{\partial u}{\partial y} = \alpha\left(u+U_b\right), \tag{3.24}$$

$$\begin{aligned} \left[1-\left(\frac{\partial \eta}{\partial y}\right)^2\right]\left(\frac{\partial v}{\partial z}+\frac{\partial w}{\partial y}\right) + 4\frac{\partial \eta}{\partial y}\frac{\partial w}{\partial z} \\ = \alpha\left\{\left[v-\left(1+\gamma\right)\frac{\partial \phi}{\partial y}\right] + \frac{\partial \eta}{\partial y}\left[w-\left(1+\gamma\right)\frac{\partial \phi}{\partial z}\right]\right\}. \end{aligned} \tag{3.25}$$

In addition to R_* and α, three additional non-dimensional parameters have been introduced:

$$S \equiv \frac{U_s(0)}{u_*}, \quad \gamma \equiv \frac{\Delta\rho}{\rho}, \quad F \equiv \frac{gh}{u_*^2}. \tag{3.26}$$

S is the normalized value of the Stokes drift velocity at the sea surface; γ is the normalized density jump across the thermocline; and F is the square of an inverse Froude number for the layer.

We close this section by estimating the order-of-magnitude of each of these non-dimensional parameters under typical oceanic conditions. Observations indicate that S can range from $O(1)$ to $O(10)$ (see e.g. Smith 1998). A typical value of γ is $O(10^{-4})$, as indicated previously. $F = O(10^6)$ for a 10–50 m deep mixed layer exposed to a $10\,\mathrm{m\,s^{-1}}$ wind (corresponding to a value of $u_* \approx 0.01\,\mathrm{m\,s^{-1}}$). Thus, the product $\gamma F = O(100)$. As suggested in Cox & Leibovich (1997), various estimates place the value of R_* between 2.5 and 50; we take R_* to be $O(1)$. Again assuming h to be $O(10)$ m and $u_* \approx 0.01\,\mathrm{m\,s^{-1}}$, this value implies $\nu_e = O(10^{-1})\,\mathrm{m^2\,s^{-1}}$; this (rather large) eddy viscosity is well within the range of estimates cited in Huang (1979). Indeed, McWilliams *et al.* (1997) extract a 'bulk eddy viscosity' greater than $O(10^{-2})\,\mathrm{m^2\,s^{-1}}$ from the results of their LES of Langmuir turbulence.

An estimate for α can be derived from typical values of w_e. The magnitude of the entrainment velocity is a function of the external parameters specifying the flow: u_*, h and γ. Thus, the normalized entrainment velocity depends on the quantity γF, an overall Richardson number characterizing the flow (Phillips 1977, p. 299). For γF between 100 and 1000 (in accord with the estimates given above), the normalized entrainment velocity, w_e/u_*, is roughly 0.01 according to the two-layer Kantha–Phillips experiment (Phillips 1977, p. 300); the numerical experiments of McWilliams *et al.* (1997) also lend credence to this value. Based on this estimate of the entrainment velocity, α ranges from 0.1 to 0.01 for ν_e ranging between 0.01 and $0.1\,\mathrm{m^2\,s^{-1}}$. With $\alpha \approx 0.1$, the hypothesized equilibrium shear flow, $\tilde{U}_b(\tilde{z})$, has a maximum velocity of

https://doi.org/10.1017/S0022112003006074 Published online by Cambridge University Press

roughly $10u_*R_* = O(0.1)\,\mathrm{m\,s^{-1}}$ – a physically reasonable value. As a final note, based on the Kantha–Phillips experiment, $w_e = O(10^{-4})\,\mathrm{m\,s^{-1}}$, which implies a relatively slow change in the mixed-layer depth of only several metres per day.

4. Asymptotic analysis

In this section, we outline an asymptotic analysis of (3.14)–(3.25) that yields analytical estimates for the Langmuir circulation growth rate, the vortex-force-modified internal-wave phase speed, and the nonlinear interaction coefficients. The derivation of these results is straightforward but algebraically involved; hence, the perturbation calculations are summarized in Appendix A; further details can be found in Chini (1999). We restrict attention to small-amplitude internal waves and Langmuir circulation maintained near marginal stability; for typical mixed-layer forcing conditions, as measured by S, the latter restriction is consistent with our use of a large-eddy viscosity (so that $R_* = O(1)$). Following Cox & Leibovich (1993), we also exploit a small-wavenumber limit, formally appropriate for internal waves and Langmuir cells having horizontal scales large compared to the mixed-layer depth. The first instability of the quasi-equilibrium shear flow is, in fact, to long-wavelength Langmuir circulation whenever the perturbation shear stresses at the air–sea interface and the mixed-layer base are small (Cox & Leibovich 1993). Here, the perturbation shear stress is assumed to vanish at the sea surface and to be proportional to α at the bottom of the mixed layer. We focus on the physically relevant scenario in which α is small because the density jump across a pre-existing thermocline is sufficiently large to permit only weak turbulent entrainment of abyssal fluid into the upper layer. As shown by Cox & Leibovich (1993), the critical Langmuir circulation wavenumber, k_{LC}^c, scales in proportion to $\alpha^{1/4}$ as $\alpha \to 0$† – also see (5.7) below.

We begin by expressing each dependent variable – for example, $u(y, z, t)$ – as the superposition of the three modes and by performing a double expansion in terms of the small-amplitude parameters, ε, δ_+ and δ_-, and the small internal-wave wavenumber, k:

$$\begin{aligned} u(y,z,t) = \varepsilon[&u_{0100}(z,T) + ku_{1100}(z,T) + k^2u_{2100}(z,T) + \ldots]\mathrm{e}^{\mathrm{i}2ky} \\ &+ \delta_+[u_{0010}(z,T) + ku_{1010}(z,T) + k^2u_{2010}(z,T) + \ldots]\mathrm{e}^{\mathrm{i}(ky-\omega t)} \\ &+ \delta_-[u_{0001}(z,T) + ku_{1001}(z,T) + k^2u_{2001}(z,T) + \ldots]\mathrm{e}^{\mathrm{i}(ky+\omega t)} \\ &+ \text{c.c.} + \text{h.o.t.} \end{aligned} \tag{4.1}$$

Here, ε is the small parameter indicative of the Langmuir circulation amplitude (i.e. the maximum cell-induced downwind current anomaly), while δ_+ and δ_- are the corresponding small parameters characterizing the amplitudes of the internal waves travelling in the positive and negative y-directions, respectively. We assume that ε, δ_+ and δ_- are of the same order of magnitude; three separate small parameters are retained simply to facilitate the bookkeeping in the perturbation analysis. (Other orderings of the small parameters, yielding different interaction equations, also may be of interest.) The four subscripts indicate the order of the given dependent variable

† In this limit, the maximum basic-state velocity must become very large – see (3.10) – since a finite flux of downwind momentum across the thermocline is required to balance the applied wind stress. Nevertheless, only the vertical gradient of the basic-state shear, rather than the maximum absolute speed, influences the downwind-invariant Langmuir-circulation and internal-wave dynamics.

https://doi.org/10.1017/S0022112003006074 Published online by Cambridge University Press

in k, ε, δ_+ and δ_-, respectively; e.g. u_{2010} arises at $O(k^2\delta_+)$. ω is the $O(k)$ internal-wave frequency; c.c. denotes complex conjugate quantities; and h.o.t. indicates higher-order (i.e. nonlinear) terms. We permit the vertical eigenfunctions to depend on a sequence of slow time scales, represented by T, in anticipation of the weak time variability that results from finite wavelength and amplitude effects. Note that the three modes satisfy the lowest-order conditions for resonance through a quadratic nonlinear interaction; namely, $k + k = 2k$ and $-\omega + \omega = 0$.

Employing the perturbation algorithm described in Appendix A, we find that the leading-order downwind velocity components satisfy $u_{0100}(z, T) = U_{0100}(T)$, $u_{0010}(z, T) = U_{0010}(T)$ and $u_{0001}(z, T) = U_{0001}(T)$, where capital letters are used to denote depth-independent dependent variables. We impose a normalization condition on the amplitude of each mode by defining the depth average of the total downwind velocity perturbation to equal the sum of the leading-order perturbations (Cox & Leibovich 1993),

$$\bar{u}(y, t) = \varepsilon U_{0100}(T)\, \mathrm{e}^{\mathrm{i}2ky} + \delta_+ U_{0010}(T)\mathrm{e}^{\mathrm{i}(ky-\omega t)} + \delta_- U_{0001}(T)\mathrm{e}^{\mathrm{i}(ky+\omega t)} + \text{c.c.}, \tag{4.2}$$

where $\bar{(\cdot)} \equiv \int_{-1}^{0}(\cdot)\mathrm{d}z$. The form of the equations governing the slow evolution of the modal amplitudes $E \equiv \varepsilon U_{0100}$, $A \equiv \delta_+ U_{0010}$ and $B \equiv \delta_- U_{0001}$ follows from symmetry considerations:

$$\frac{\mathrm{d}E}{\mathrm{d}t} = \sigma E + e_{nr} A B, \tag{4.3}$$

$$\frac{\mathrm{d}A}{\mathrm{d}t} = (a_{lr} + \mathrm{i}a_{li})A + (a_{nr} + \mathrm{i}a_{ni})E B^*, \tag{4.4}$$

$$\frac{\mathrm{d}B}{\mathrm{d}t} = (a_{lr} - \mathrm{i}a_{li})B + (a_{nr} - \mathrm{i}\,a_{ni})E A^*. \tag{4.5}$$

The coefficients, however, must be determined by carrying out the perturbation analysis.

5. Results

As discussed in § 1, we have performed an asymptotic analysis of a simple ocean model primarily to derive physical insight. We now summarize the results of our linear and nonlinear analysis, highlighting the simple physical mechanisms revealed by the theory.

5.1. *Vortex-force-modified linear internal-wave dynamics*

Using the expressions for the linear Langmuir-circulation ('*LC*') and internal-wave ('*IW*+') fields given in Appendix A.1, we now describe the long-wavelength kinematics of these modes. As expected for a thin fluid layer, the leading-order Langmuir-circulation and internal-wave pressure perturbations are depth-independent, and the vertical velocity perturbations are $O(k)$ relative to the (horizontal) cross-wind flows. The results given in Appendix A.1 indicate that a *stationary* depth-independent cross-wind-periodic $O(\varepsilon)$ x-velocity perturbation, u_{LC}, drives an $O(\varepsilon k)$ horizontal vortex-force component that decays linearly with depth and is directed toward planes of maximum (positive) u_{LC}. To conserve mass, a depth-independent cross-wind-periodic $O(\varepsilon)$ pressure perturbation, $\pi_{LC} = (S/2)u_{LC}$, is induced, with maximum (positive) pressures coinciding with planes of maximum u_{LC} (see figure 2*a*). The associated depth-independent $O(\varepsilon k)$ cross-wind pressure gradient opposes the horizontal vortex-force component. Near the air–sea interface, the vortex force is sufficiently strong

https://doi.org/10.1017/S0022112003006074 Published online by Cambridge University Press

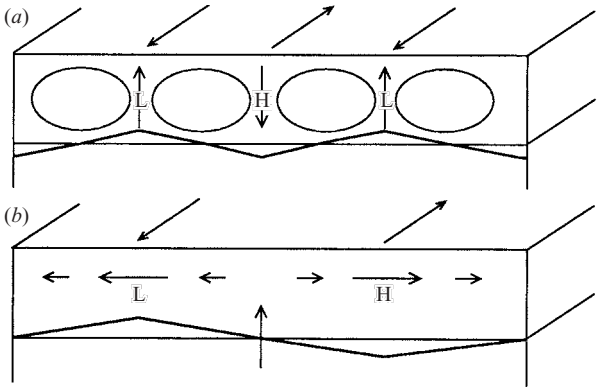


FIGURE 2. Kinematics of long-wavelength stationary Langmuir circulation (upper) and cross-wind propagating internal waves (lower). The upper-layer pressure is independent of depth, with 'H' and 'L' denoting regions of high and low pressure, respectively. The horizontal vortex-force component induced by downwind current anomalies opposes cross-wind pressure gradients, thereby driving cellular motions in the case of the Langmuir circulation and reducing the phase speed of cross-wind travelling internal waves.

to overcome this pressure gradient, driving an $O(\varepsilon k)$ horizontal cross-wind flow, v_{LC}, toward planes of maximum u_{LC}. At the base of the upper layer, however, the vortex force is weak (since the Stokes drift decays with depth), and the pressure gradient drives fluid away from these planes, with cellular motions emerging at $O(\varepsilon k^2)$. Near the marginal stability threshold, transport of basic-state momentum by this cellular flowfield maintains the Langmuir circulation against viscous dissipation. Finally, we note that the vortex-force induced $O(\varepsilon)$ pressure perturbations deform the thermocline: $\eta_{LC} = -\pi_{LC}/(\gamma F) = -u_{LC}\, S/(2\gamma F)$, so the thermocline is depressed beneath Langmuir-circulation downwind surface jets.

An interesting feature which emerges from our analysis (see Appendix A.1) is the way in which the CL vortex force modifies the *linear* dynamics of cross-wind propagating internal waves – even in the absence of a nonlinear interaction with Langmuir circulation. One manifestation of this vortex-force effect is a reduction in the phase speed of cross-wind propagating internal waves,

$$\omega = k\left[\gamma F - \frac{R_* S}{4}\right]^{1/2}, \tag{5.1}$$

as indicated by the presence of the Stokes drift parameter S in (5.1); this result is in qualitative agreement with Thorpe (1997). The reduction in phase speed is not a simple advection effect, since the internal waves propagate in a direction normal to the Stokes drift (see figure 1). Instead, an imposed $O(\delta_+)$ time-periodic cross-wind-periodic deflection of the thermocline, η_{IW+}, with frequency $\omega = O(k)$ and $O(\delta_+)$ depth-independent pressure perturbations, π_{IW+}, drives an $O(\delta_+)$ horizontal and $O(\delta_+ k)$ vertical cross-wind flow field. Vertical advection of the basic-state shear creates cross-wind-periodic downwind velocity anomalies, u_{IW+}, with a depth-independent component arising at $O(\delta_+)$ and a vertically varying component (with zero depth average) arising at $O(\delta_+ k)$. Although negative anomalies are initiated above internal-wave upwelling sites, there is a phase lag associated with the vertical advection of basic-state momentum; consequently, cross-wind minima of u_{IW+} are aligned with internal-wave crests, while maxima are aligned with internal-wave troughs, as depicted

https://doi.org/10.1017/S0022112003006074 Published online by Cambridge University Press

in the lower schematic of figure 2. In the absence of the vortex force, these downwind velocity perturbations would not feed back upon the (downwind-invariant) cross-wind flow. In the presence of an x-directed surface-wave Stokes drift, however, an $O(\delta_+ k)$ horizontal vortex-force component is induced. This vortex-force component is directed toward planes of maximum (positive) downwind velocity perturbations – as in the case of the Langmuir circulation. Thus, the cross-wind pressure gradient and, hence, the internal wave phase speed are reduced.

The distinction between the internal-wave and Langmuir circulation modes is blurred slightly because of the influence of the vortex force. For example, both modes exhibit $O(\varepsilon k^2)$ cellular motions (taking $\varepsilon \equiv \delta_+$). However, the modes are distinguished by the relative size of the cross-wind velocity fields: $O(v_{LC}) = O(k v_{IW+})$ and $O(w_{LC}) = O(k w_{IW+})$, for $O(u_{LC}) = O(u_{IW+})$. Moreover, even though the internal-wave vertical velocity is non-zero at $O(\delta_+ k)$, cellular motions do not arise at this order. Most significantly, the time-dependence of (propagating or standing) internal waves evidently inhibits the feedback mechanism that sustains the stationary Langmuir circulation, so free internal waves are damped due to the non-zero upper-layer viscosity. Nevertheless, we emphasize that the vortex-force-modified internal-wave dynamics play a central role in the nonlinear interaction between Langmuir circulation and resonant cross-wind propagating internal waves.

5.2. *Linear stability characteristics*

In the small-α limit, the Langmuir circulation growth rate, σ, must be $O(k^4)$ if spatial amplitude modulation is to be incorporated in a consistent manner (Cox & Leibovich 1993). Although we do not consider spatial modulation in this work, we have extended our analysis to $O(k^4)$ – see (A 13) – to compare the linear stability characteristics of wind-driven shear flows above sharp-compliant and rigid-planar thermoclines. Setting

$$R_*^3 S \equiv 120 + P, \quad P = O(k^2), \tag{5.2}$$

and defining $k_{LC} \equiv 2k$, we find

$$\sigma = \frac{R_* \gamma F}{(R_*^2 \gamma F - 30)} \left[-\alpha \left(1 - \frac{60}{R_*^2 \gamma F} \right) + \frac{P}{120} k_{LC}^2 - \frac{1091}{5544} k_{LC}^4 \right], \tag{5.3}$$

where $\alpha = O(k^4)$. The growth rate of large aspect-ratio Langmuir cells above a planar thermocline may be recovered by taking the limit of (5.3) as $\gamma \to \infty$ (cf. Cox & Leibovich 1993):

$$\lim_{\gamma \to \infty} \sigma \equiv \sigma_{\gamma \to \infty} = \frac{1}{R_*} \left[-\alpha + \frac{P}{120} k_{LC}^2 - \frac{1091}{5544} k_{LC}^4 \right]. \tag{5.4}$$

The expressions for the growth rates given in (5.3) and (5.4) are both purely real: Langmuir cells in a homogeneous layer of fluid are born in a stationary bifurcation, whether the thermocline bounding that layer is assumed to be rigid or deformable (at least in the small-α, i.e. large aspect-ratio, limit and in the absence of background rotation). Forming the ratio of (5.3) to (5.4),

$$\frac{\sigma}{\sigma_{\gamma \to \infty}} = \left[\frac{1}{1 - \left(\dfrac{30}{R_*^2 \gamma F} \right)} \right] \left\{ 1 + \left(\frac{60 \alpha}{-\alpha + \dfrac{P}{120} k_{LC}^2 - \dfrac{1091}{5544} k_{LC}^4} \right) \frac{1}{R_*^2 \gamma F} \right\}, \tag{5.5}$$

https://doi.org/10.1017/S0022112003006074 Published online by Cambridge University Press

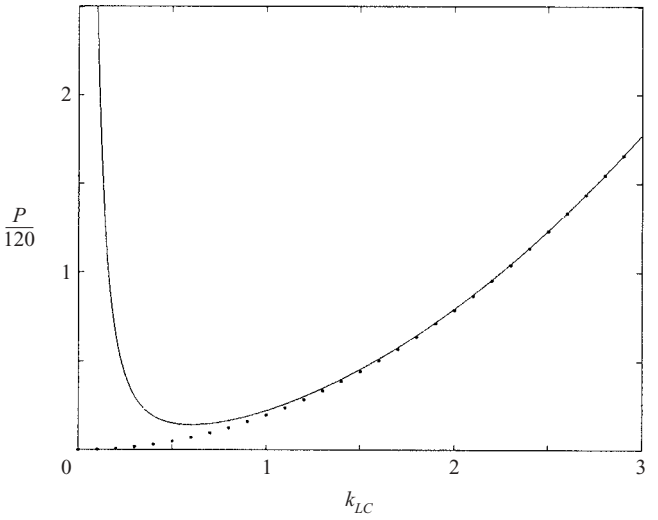


FIGURE 3. Langmuir circulation marginal stability curves for $R_* = 2$, $\gamma F = 100$, and $\alpha = 0$ (dotted curve) and $\alpha = 0.03$ (solid curve). When $\alpha = 0$, the first disturbance to be amplified as the 'reduced forcing' ($P/120$) increases through zero has an infinite wavelength (i.e. zero wavenumber). For finite α, the first disturbance to be amplified (as the reduced forcing is increased through some finite value) has a finite wavenumber. However, if α is small, so too is this critical wavenumber.

where the term in braces is $\{1+O(1/R_*^2\gamma F)\}$, it is evident that the Langmuir circulation growth rate is amplified by the compliance of the thermocline. Consideration of the expression for the $O(k)$ internal-wave frequency, (5.1), suggests that a bifurcation occurs when $\gamma F/R_* S$ is less than $1/4$ – or, equivalently, when $R_*^2\gamma F/30 < 1$ for $R_*^3 S = 120 + O(k^2)$. The two-layer system is then unstable to large-scale Langmuir cells having zero phase speed and exponential (i.e. finite rather than infinite) real growth rate $\sigma = k(R_* S/4 - \gamma F)^{1/2}$. Here, we restrict attention to $R_*^2\gamma F = O(100)$, so these modes (which would cause complete overturning of the thermocline) are not realized. The resulting amplification of the Langmuir circulation growth rate is modest, though not negligible; σ is increased by almost 50% relative to the rigid thermocline scenario.

The wavenumber of the fastest-growing linear mode, k_{LC}^f, is readily obtained by setting the derivative of (5.3) with respect to k_{LC} to zero and solving for k_{LC}^f:

$$k_{LC}^f = \sqrt{\left(\frac{2772}{1091}\right)\left(\frac{P}{120}\right)}. \tag{5.6}$$

Thus, in the small-wavenumber limit, k_{LC}^f is independent of the magnitude of both the density jump across the thermocline and the turbulent entrainment velocity, instead depending only on $P/120$, the 'reduced' forcing parameter. The marginal stability curve shown in figure 3 is obtained by setting $\sigma = 0$ in (5.3). Its minimum occurs at a critical wavenumber

$$k_{LC}^c = \left\{\alpha\left(\frac{5544}{1091}\right)\left[1 - \frac{60}{R_*^2\gamma F}\right]\right\}^{1/4} \tag{5.7}$$

https://doi.org/10.1017/S0022112003006074 Published online by Cambridge University Press

and 'critical reduced forcing'

$$\frac{P^c}{120} = \sqrt{\alpha \frac{4364}{5544}\left[1 - \frac{60}{R_*^2 \gamma F}\right]}. \tag{5.8}$$

From (5.7) and (5.8), we observe that the compliance of the thermocline reduces both the critical wavenumber and the critical reduced forcing. In fact, as $R_*^2 \gamma F \to 60$, both P^c and k_{LC}^c tend to zero, independently of α. We note that Pavithran & Redekopp (1994) obtained a similar result in their analysis of thermal convection with a deformable surface; they found that the critical wavenumber and Rayleigh number pass through zero as the density jump across the deformable interface is reduced through a finite value. We emphasize, as they do, that the presence of the deformable interface enhances the onset of convective activity.

5.3. *Resonant nonlinear internal-wave reflection*

The resonant interaction equations can be obtained by using the expressions for the slow time derivatives of the modal amplitudes: (A 14), (A 20), (A 21) and (5.3). Recalling that $\varepsilon \equiv \delta_+ \equiv \delta_-$, setting $\varepsilon \equiv k$ and retaining only those terms which are cubic in the combined small parameters, we obtain the following asymptotically consistent set of lowest-order resonant interaction equations:

$$\frac{\mathrm{d}E}{\mathrm{d}t} = 0, \tag{5.9}$$

$$\frac{\mathrm{d}A}{\mathrm{d}t} = (a_{lr} + \mathrm{i}a_{li})A + \mathrm{i}a_{ni} E B^*, \tag{5.10}$$

$$\frac{\mathrm{d}B}{\mathrm{d}t} = (a_{lr} - \mathrm{i}a_{li})B - \mathrm{i}a_{ni} E A^*. \tag{5.11}$$

By employing long-wavelength asymptotics, we have obtained closed-form expressions for the linear and nonlinear coefficients in the resonant interaction equations as functions of k, R_*, α, γ, F and S. For example, the real linear coefficient,

$$a_{lr} = -k^2\left(\frac{3}{2R_*}\right), \tag{5.12}$$

gives the internal-wave damping rate. This damping rate is proportional to the eddy viscosity, implying that the internal waves lose energy to the upper-layer turbulence. In fact, our use of an order-unity R_* yields an unrealistically large damping rate. The experimental results of Ostrovsky *et al.* (1996), for example, suggest an internal-wave damping rate at least an order of magnitude less than that obtained from (5.12); open-ocean damping rates may be expected to be even smaller, owing to the absence of boundary effects. Estimation of energy transfers between internal waves and small-scale turbulent fluctuations clearly requires sophisticated modelling of the incoherent turbulence (see e.g. the modelling work of Ostrovsky & Zaborskikh 1996) – the constant eddy-viscosity assumption employed here is grossly inadequate. Hereinafter, we set the internal-wave damping rate $a_{lr} = o(k^2)$, a closer approximation to observations than (5.12). The imaginary linear coefficient,

$$a_{li} = k^2 c\left(\frac{1+\gamma}{2}\right), \tag{5.13}$$

https://doi.org/10.1017/S0022112003006074 Published online by Cambridge University Press

where $c \equiv \omega/k$ is the leading-order internal wave phase speed, represents a dispersive phase-speed reduction: $c \mapsto c[1-(k/2)(1+\gamma)]$. The imaginary nonlinear coefficient,

$$a_{ni} = -k\left[\frac{90(R_*^2\gamma F - 60)}{R_*^4\gamma F(R_*^2\gamma F - 30)^{1/2}}\right], \tag{5.14}$$

accounts for the interaction between the propagating internal waves and the stationary Langmuir circulation. Note that, for large γF,

$$a_{ni} \to -k\,\frac{90}{R_*^3(\gamma F)^{1/2}} = -k\frac{3S}{4(\gamma F)^{1/2}} \tag{5.15}$$

using (5.2); we identify the physical origin of this scaling below.

Equation (5.9) indicates that the Langmuir circulation is unaffected by the presence of the internal waves, at least over the $O(k^{-2})$ time scale considered. Indeed, (A 20) and (A 21) imply that e_{nr} and a_{nr} are $o(k)$, indicating that there is no energy exchange between the Langmuir circulation and the internal waves over this time scale. (In a companion article, we show that e_{nr} and a_{nr} are $O(k^2)$ by extending our analysis to $O(k^2\delta_+\delta_-)$, $O(k^2\varepsilon\delta_-)$.) Instead, the vortices simply mediate a conservative energy exchange between the counter-propagating waves.

This result can readily be seen by integrating (5.10) and (5.11) with $E = E_0$ (a constant). After scaling out the linear terms via the transformations $\tilde{A} \equiv A\exp(-(a_{lr}+\mathrm{i}a_{li})t)$, $\tilde{B} \equiv B\exp(-(a_{lr}-\mathrm{i}a_{li})t)$, we obtain

$$\tilde{A} = A_+\exp(\mathrm{i}a_{ni}|E_0|t) + A_-\exp(-\mathrm{i}a_{ni}|E_0|t), \tag{5.16}$$

$$\tilde{B} = B_+\exp(\mathrm{i}a_{ni}|E_0|t) + B_-\exp(-\mathrm{i}a_{ni}|E_0|t), \tag{5.17}$$

where $B_+ \equiv -A_-^*E_0/|E_0|$ and $B_- \equiv A_+^*E_0/|E_0|$. This solution is displayed in figure 4. Figure 4(*a*) clearly shows a conservative exchange of energy between the counter-propagating internal waves, a dynamic more vividly depicted by the spatio-temporal evolution of the internal-wave-induced interfacial displacement (see figure 4*b*). Lines of constant phase initially are aligned in the direction of increasing y and increasing t, corresponding to a positively propagating wave. Although initially zero, the amplitude of the negatively propagating wave grows owing to the nonlinear interaction between the positive wave and the Langmuir circulation. At a non-dimensional time of approximately six, the magnitudes of the wave amplitudes are roughly equal; the superposition of the two waves then forms an approximate standing-wave pattern. Subsequently, the energy of the negative wave dominates, and the lines of constant phase reorient in the direction of decreasing y and increasing t. This process repeats – indefinitely, in fact – not only because internal-wave damping has been neglected, but also because spatial amplitude modulation has not been incorporated. Thus, the internal waves cannot 'escape' from the infinite field of Langmuir cells. By extending our analysis to account for spatial modulation, we have been able to investigate the transmission and reflection of internal-wave packets incident upon a Langmuir circulation field of finite horizontal extent; the results of these calculations will be reported elsewhere.

The central result of this investigation is that cross-wind propagating internal waves can be resonantly reflected from a stationary Langmuir circulation field. The oscillation frequency is proportional to the product of the Langmuir-circulation amplitude and the nonlinear interaction coefficient a_{ni}, which itself is proportional to k. For the parameters used in figure 4, the oscillation period is $O(10)$ h. The required 2:1 wavelength-relationship for resonance suggests that the dynamic is akin to the

https://doi.org/10.1017/S0022112003006074 Published online by Cambridge University Press

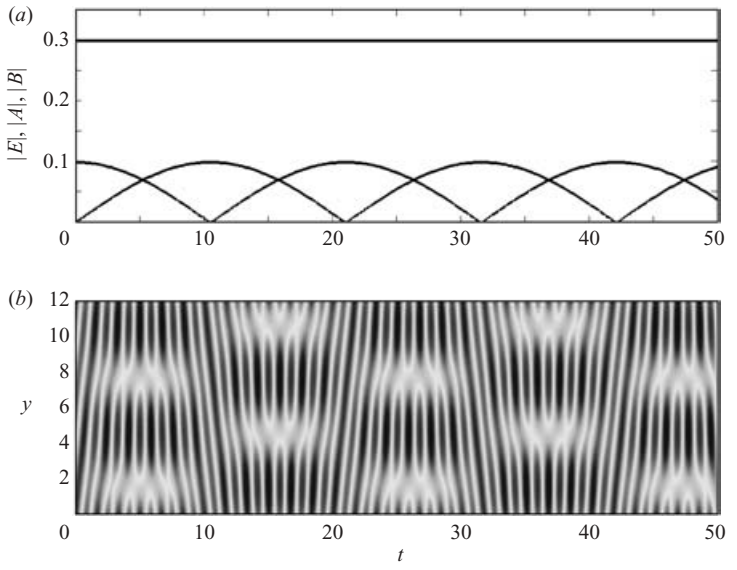


FIGURE 4. Internal-wave reflection from Langmuir circulation. $k = 0.5$, $R_* = 2$, $S = 15$ and $\gamma F = 100$. (*a*) The conservative oscillation in the internal-wave amplitudes. The Langmuir circulation amplitude remains constant; the cells simply mediate the energy exchange between the counter-propagating waves. (*b*) A reconstruction of the interfacial displacement field induced solely by the internal waves. The sequence of reflections is evident by the changing orientation of lines of constant phase.

'Bragg reflection' of, for example, surface waves propagating over sand bars (Mei 1985), although the physical mechanism differs.

The reflection mechanism can be understood by first noting that the dominant contribution to a_{ni} is from the advection term $v_{IW}\partial u_{LC}/\partial y$, which accounts for approximately two-thirds of the coefficient given in (5.15). Consider an internal wave of wavenumber k and frequency ω propagating in (say) the negative cross-wind direction past a field of stationary Langmuir cells having wavenumber $2k$ and axes aligned with the wind direction. The cross-wind velocity field, v_{IW-}, associated with the internal wave advects the downwind current anomalies, u_{LC}, created by the Langmuir cells. Since $v_{IW-} \propto \exp[-\mathrm{i}(ky + \omega t)]$ and $u_{LC} \propto \exp[\mathrm{i}\,2ky]$, a pattern of downwind current anomalies, u_{IW+}, is created with wavenumber k and phase speed $c = \omega/k$ in the positive cross-wind direction. From the balance $\partial u_{IW+}/\partial t \approx -v_{IW-}\partial u_{LC}/\partial y$, the scaling

$$u_{IW+} \propto \omega^{-1} v_{IW-} k\, u_{LC} \tag{5.18}$$

is obtained. The propagating vertical vorticity perturbations $\partial u_{IW+}/\partial y$ induce a horizontal vortex-force distribution that drives a cross-wind flow, as described in § 5.1. This horizontal vortex-force, which scales in proportion to Sku_{IW+}, transfers energy to the reflected wave by doing work on particle displacements induced by the wave. The rate at which this energy is transferred scales as the product of the vortex force and the reflected-wave cross-wind velocity v_{IW+}:

$$\mathscr{P} \propto Sku_{IW+}v_{IW+}, \tag{5.19}$$

where $\mathscr{P}$ is the power transferred. The energy of the reflected wave is proportional to v_{IW+}^2; from (A 12), $v_{IW+} = O(cu_{IW+}/R_*)$, so $\mathscr{E} \propto [cu_{IW+}/R_*]^2$, where $\mathscr{E}$ is the energy

https://doi.org/10.1017/S0022112003006074 Published online by Cambridge University Press

of the wave. Since $\mathrm{d}\mathscr{E}/\mathrm{d}t = \mathscr{P}$, the rate of growth of the square of the reflected-wave downwind velocity is given by R_*^2/c^2 multiplied by $\mathscr{P}$. Using (5.18) and (5.19), the implied interaction coefficient scales in proportion to kS/c. For sufficiently large γF, this scaling estimate agrees with the form of the interaction coefficient given in (5.15).

6. Conclusion

A two-layer model has been used to study the influence of thermocline compliance on the dynamics of Langmuir circulation in the oceanic mixed layer. The assumptions in our asymptotic theory preclude quantitative comparison of model results with oceanographic observations. For example, the restriction to weak nonlinearity suggests that the interaction time scale is very likely to be over-estimated by our analysis. Similarly, the representation of turbulent Langmuir vortices as neutral two-dimensional eigenfunctions of a quasi-laminar stability problem is an extreme simplification; our rationale is that Langmuir cells are the dominant structures in the fully turbulent mixed layer and, as such, are maintained by a hydrodynamic-instability mechanism whose broad features we correctly capture. The strongly nonlinear evolution of these coherent structures is, of course, far more complex. Our neglect of Coriolis accelerations is justified only when the time scale for the Langmuir-circulation–internal-wave interaction is small compared to the inverse of the Coriolis parameter, $f \equiv 2\Omega \sin \Lambda$, where Ω is the rotation rate of the earth and Λ is the latitude of the local water column. Thus, our analysis is likely to be most applicable to the dynamics of equatorial or tropical waters; not only does f tend to zero as the equator is approached, but pre-existing sharp thermoclines are more prevalent in tropical regions. Finally, open-ocean observations suggest that the dominant Langmuir circulation wavelength is roughly three times the mixed-layer depth rather than an asymptotically large distance (Smith, Pinkel & Weller 1987). Fortuitously, Cox & Leibovich (1993) and Cox (1997) demonstrate that the small-wavenumber asymptotics remains quantitatively accurate (at least close to the instability threshold) even for wavenumbers approaching unity – and that is our hope here. The actual (rather than formal) range of validity of the asymptotic model ultimately should be assessed by comparisons with numerical simulations of the primitive equations.

Our purpose, rather, has been to identify qualitative differences between the dynamics of wind-driven mixed layers bounded below by compliant and rigid thermoclines and to elucidate the physical mechanisms responsible for those differences. We briefly summarize our key results. First, thermocline compliance enhances the growth rate of Langmuir cells, but does not (in the large aspect-ratio limit, at least) change the nature of the bifurcation: the cells are born in a stationary, rather than Hopf, bifurcation. Next, the dynamics of low-mode internal waves, propagating along the thermocline in the cross-wind direction, are modified by the vortex force arising from the interaction of surface waves with the wind-driven shear. Since the early work of Craik & Leibovich (1976), the role of the vortex force in the generation of Langmuir circulation has gained wide acceptance; however, its role in modifying other aspects of time-averaged upper-ocean dynamics – e.g. internal-wave propagation – is, perhaps, less well appreciated. The vortex force fully couples downwind and cross-wind motions, even when all (time-averaged) flows are invariant in the downwind direction, as in this investigation. Consequently, cross-wind travelling internal waves experience a reduction in phase speed, because the vortex

https://doi.org/10.1017/S0022112003006074 Published online by Cambridge University Press

force induced by the internal-wave motion opposes the cross-wind pressure gradient driving the wave.

The vortex-force modification of the (linear) internal-wave dynamics is crucial to the central result of this investigation; namely, that cross-wind propagating internal waves can be nonlinearly reflected from a stationary Langmuir circulation field, if the wavelength of the internal waves is twice that of the Langmuir circulation – that is, if a Bragg resonance condition is satisfied. As an incident internal wave propagates past the stationary cells, the wave's cross-wind horizontal velocity advects the Langmuir-cell downwind current anomalies. The result is a pattern of downwind current anomalies propagating with the same phase speed and wavelength as the incident wave, but in the opposite direction. The vortex force induced by the vertical vorticity perturbations associated with the propagating downwind current anomalies drives cross-wind velocity perturbations. Together, the downwind and cross-wind flows comprise a reflected (vortex-force modified) internal wave. Over the time scale characterizing this reflection process, the Langmuir circulation mediates a conservative transfer of energy between counter-propagating internal waves, but is otherwise unaffected by the interaction. Energy exchanges between the Langmuir circulation and internal waves occur over a longer time scale and give rise to more complex mixed-layer dynamics.

This work was supported by the US Navy under contracts ONR N00014-93-1-0476 and ONR AASERT N00014-95-1-0820. G. P. C. also gratefully acknowledges the support he received from an NDSEG fellowship administered through the US Navy.

Appendix A. Perturbation calculations

Equation (3.18) can be solved immediately; the solution satisfying the large-depth condition (3.20) is:

$$\begin{aligned}\phi(y,z,t) = \varepsilon\ & [\Phi_{0100}(T) + k\Phi_{1100}(T) + \ldots]\ \mathrm{e}^{\mathrm{i}2ky}\,\mathrm{e}^{2k(z+1)} \\ & + \delta_+\ [\Phi_{0010}(T) + k\Phi_{1010}(T) + \ldots]\ \mathrm{e}^{\mathrm{i}(ky-\omega t)}\,\mathrm{e}^{k(z+1)} \\ & + \delta_-\ [\Phi_{0001}(T) + k\Phi_{1001}(T) + \ldots]\ \mathrm{e}^{\mathrm{i}(ky+\omega t)}\,\mathrm{e}^{k(z+1)} + \text{c.c.} + \text{h.o.t.} \qquad (A\,1)\end{aligned}$$

A.1. *Linear analysis*

Upon linearization, the partial differential equations, (3.14)–(3.17), boundary conditions, (3.19)–(3.20), and interfacial conditions, (3.21)–(3.25), become:

$$\frac{\partial w}{\partial z} = -\frac{\partial v}{\partial y}, \qquad (A\,2)$$

$$\frac{1}{R_*}\frac{\partial^2 u}{\partial z^2} = \frac{\partial u}{\partial t} + R_* w - \frac{1}{R_*}\frac{\partial^2 u}{\partial y^2}, \qquad (A\,3)$$

$$\frac{1}{R_*}\frac{\partial^2 v}{\partial z^2} = \frac{\partial v}{\partial t} + \frac{\partial \pi}{\partial y} - S(1+z)\,\frac{\partial u}{\partial y} - \frac{1}{R_*}\frac{\partial^2 v}{\partial y^2}, \qquad (A\,4)$$

$$\frac{\partial \pi}{\partial z} = S(1+z)\,\frac{\partial u}{\partial z} - \frac{\partial w}{\partial t} + \frac{1}{R_*}\left(\frac{\partial^2 w}{\partial z^2} + \frac{\partial^2 w}{\partial y^2}\right), \qquad (A\,5)$$

https://doi.org/10.1017/S0022112003006074 Published online by Cambridge University Press

and

$$w(y,0,t)=0, \quad w(y,-1,t) = \frac{\partial \eta}{\partial t}(y,t), \tag{A 6a,b}$$

$$\frac{\partial u}{\partial z}(y,0,t)=0, \quad \frac{\partial u}{\partial z}(y,-1,t) = \alpha u(y,-1,t)+\alpha R_* \eta(y,t), \tag{A 7a,b}$$

$$\frac{\partial v}{\partial z}(y,0,t)=0,$$

$$\frac{\partial v}{\partial z}(y,-1,t) = -\frac{\partial w}{\partial y}(y,-1,t)+\alpha\left[v(y,-1,t)-(1+\gamma)\frac{\partial \phi}{\partial y}(y,-1,t)\right], \tag{A 8a,b}$$

$$\pi(y,-1,t) = -\gamma F \eta(y,t)+\frac{2}{R_*}\frac{\partial w}{\partial z}(y,-1,t) - (1+\gamma)\frac{\partial \phi}{\partial t}(y,-1,t), \tag{A 9}$$

$$\frac{\partial \phi}{\partial z}(y,-1,t) = \frac{\partial \eta}{\partial t}(y,t), \tag{A 10}$$

where the form of (A 2)–(A 10) suggests the algorithm for the perturbation calculation.

We proceed by omitting h.o.t. from (4.1) and substituting the truncated expansion into the linearized system (A 2)–(A 10). The vertical eigenfunctions depend on the slow time scales $T_{20}\equiv k^2 t$, $T_{30}\equiv k^3 t$ and $T_{40}\equiv k^4 t$ (where the first subscript indicates the order in k, and the second refers to the order in one of the small-amplitude parameters), implying

$$\frac{\partial}{\partial t} \longmapsto \frac{\partial}{\partial t}+k^2\frac{\partial}{\partial T_{20}} + k^3\frac{\partial}{\partial T_{30}}+k^4\frac{\partial}{\partial T_{40}}.$$

A sequence of linear inhomogeneous problems is generated at $O(\varepsilon k^n)$ and $O(\delta_+ k^n)$, where $n \geqslant 0$. When $n=0$, $u_{0100}(z,T)$ satisfies $\partial^2 u_{0100}(z,T)/\partial z^2 = 0$ subject to $\partial u_{0100}(z,T)/\partial z = 0$ at $z=0$ and $z=-1$ (and similarly for $u_{0010}(z,T)$), which has the non-trivial solution $u_{0100}(z,T)=U_{0100}(T)$, an arbitrary function of T. Thus, the linear operator has a zero eigenvalue, and the sequence of problems can only be solved if certain solvability conditions are satisfied. Non-trivial solvability conditions determine the Langmuir circulation growth rate and the internal-wave phase speed.

Although analytically tractable, the perturbation calculations become unwieldy beyond $O(\varepsilon k)$ and $O(\delta_+ k)$. For this reason, the symbolic algebra package *Maple* was used to complete the calculations; see Appendix B of Chini (1999) for details. Here, we simply summarize the main results. The leading-order linear Langmuir-circulation fields are:

$$\left.\begin{aligned} u_{0100} = U_{0100}, \quad \pi_{0100} = \frac{S}{2}U_{0100}, \quad \eta_{0100} = -\frac{S}{2\gamma F}U_{0100}, \\ v_{1100} = \mathrm{i}R_* S\left(\frac{1}{12}-\frac{z^2}{2}-\frac{z^3}{3}\right)U_{0100}, \quad w_{2100} = R_* S\left(\frac{z}{6}-\frac{z^3}{3}-\frac{z^4}{6}\right)U_{0100}. \end{aligned}\right\} \tag{A 11}$$

The leading-order linear (positively-propagating) internal-wave fields are:

$$\left.\begin{aligned} u_{0010} = U_{0010}, \quad v_{0010} = \frac{2c}{R_*}U_{0010}, \quad w_{1010} = -\mathrm{i}\left(\frac{2c}{R_*}\right)zU_{0010}, \\ \pi_{0010} = \frac{2\gamma F}{R_*}U_{0010}, \quad \eta_{0010} = -\frac{2}{R_*}U_{0010}, \quad \Phi_{0010} = \mathrm{i}\left(\frac{2c}{R_*}\right)U_{0010}. \end{aligned}\right\} \tag{A 12}$$

https://doi.org/10.1017/S0022112003006074 Published online by Cambridge University Press

The $O(\varepsilon k^2)$, $O(\varepsilon k^3)$ and $O(\varepsilon k^4)$ solvability conditions require:

$$\frac{\partial U_{0100}}{\partial T_{20}} = \frac{\gamma F}{30 R_* c^2}\left[R_*^3 S - 120\right] U_{0100}, \tag{A 13a}$$

$$\frac{\partial U_{0100}}{\partial T_{30}} = 0, \tag{A 13b}$$

$$\frac{\partial U_{0100}}{\partial T_{40}} = \left(\frac{\gamma F}{R_* c^2}\right)\left[\frac{\alpha}{k^4}\left(\frac{60}{R_*^2 \gamma F} - 1\right) - \frac{2182}{693}\right] U_{0100}, \tag{A 13c}$$

where $\alpha = O(k^4)$. The $O(\delta_+ k)$, $O(\delta_+ k^2)$ and $O(\delta_+ k^3)$ solvability conditions require:

$$\omega = k\left[\gamma F - \frac{R_* S}{4}\right]^{1/2}, \tag{A 14a}$$

$$\frac{\partial U_{0010}}{\partial T_{20}} = \left\{-\left[\frac{3}{2 R_*}\right] + \mathrm{i}\, c\left[\frac{(1+\gamma)}{2}\right]\right\} U_{0010}, \tag{A 14b}$$

$$\frac{\partial U_{0010}}{\partial T_{30}} = \left\{\frac{3}{2}\left[\frac{(1+\gamma)}{R_*}\right] + \mathrm{i}\left(\frac{1}{56 R_*^2 c}\right)\left[(383 + 1260\gamma + 630\gamma^2) - R_*^2 \gamma F\left(\frac{53}{6} + 42\gamma + 21\gamma^2\right)\right]\right\} U_{0010}. \tag{A 14c}$$

A.2. *Nonlinear analysis*

To complete the derivation of the interaction equations, we include resonant quadratic nonlinear terms in the expansion (4.1); that is, we retain terms of the form

$$\delta_+\delta_- \mathrm{e}^{\mathrm{i}2ky},\ \varepsilon\delta_+ \mathrm{e}^{\mathrm{i}(ky+\omega t)},\ \varepsilon\delta_- \mathrm{e}^{\mathrm{i}(ky-\omega t)},$$

as well as the complex conjugates of these terms (which will be denoted with asterisks). Furthermore, we retain the quadratic nonlinear terms in equations (3.14)–(3.16) and in the Taylor series expansions of the interfacial boundary conditions, (3.21)–(3.25), about $z = -1$. For example, when expanded, (3.24) becomes:

$$\left\{\left[1 + \eta(y,t)\frac{\partial}{\partial z} + \cdots\right]\frac{\partial u}{\partial z}\right\}_{(y,-1,t)} - \frac{\partial \eta(y,t)}{\partial y}\left\{\left[1 + \eta(y,t)\frac{\partial}{\partial z} + \cdots\right]\frac{\partial u}{\partial y}\right\}_{(y,-1,t)} = \alpha\left\{\left[1 + \eta(y,t)\frac{\partial}{\partial z} + \cdots\right]u\right\}_{(y,-1,t)} + \alpha\,\eta(y,t)\frac{\mathrm{d}U_b}{\mathrm{d}z}(-1). \tag{A 15}$$

Since the nonlinearity in the governing equations and interfacial conditions invalidates the exponential time-dependence ansatz, we introduce an additional slow time scale,

$$T_{11} \equiv k\varepsilon t = k\delta_+ t = k\delta_- t, \tag{A 16}$$

to permit the modal amplitudes to exhibit more complex temporal behaviour. Thus, $U_{0100}(T_{20}, T_{30}, T_{40}) \longmapsto U_{0100}(T_{11}, T_{20}, T_{30}, T_{40})$, etc., and all time-derivatives transform according to:

$$\frac{\partial}{\partial t} \longmapsto \frac{\partial}{\partial t} + k\varepsilon\frac{\partial}{\partial T_{11}} + k^2\frac{\partial}{\partial T_{20}} + k^3\frac{\partial}{\partial T_{30}} + k^4\frac{\partial}{\partial T_{40}}, \tag{A 17}$$

where, again, $\varepsilon \equiv \delta_+ \equiv \delta_-$, as implied by (A 16). The perturbation algorithm is analogous to that followed in Appendix A.1. Rather than determining finite-wavelength

https://doi.org/10.1017/S0022112003006074 Published online by Cambridge University Press

corrections to σ and ω, the solvability conditions that arise yield the nonlinear coupling coefficients in the resonant interaction equations. Again, the calculations are lengthy, and we merely summarize the key steps and results. At $O(\delta_+\delta_-)$, we find for the Langmuir circulation:

$$w_{0011} = 0, \quad u_{0011} = 0, \quad v_{0011} = V_{0011}, \quad \pi_{0011} = \Pi_{0011},$$
$$\eta_{0011} = -\frac{\Pi_{0011}}{\gamma F} - \frac{R_* S}{\gamma F}\,\eta_{0010}\,\eta_{0001}. \tag{A 18}$$

The corresponding internal-wave fields, at $O(\varepsilon\delta_-)$, are:

$$w_{0101} = 0, \quad u_{0101} = 0, \quad v_{0101} = V_{0101}, \quad \pi_{0101} = \Pi_{0101},$$
$$\eta_{0101} = -\frac{\Pi_{0101}}{\gamma F} - \frac{R_* S}{\gamma F}\,\eta_{0100}\,\eta^*_{0001}. \tag{A 19}$$

The $O(k\delta_+\delta_-)$ solvability condition for the Langmuir circulation,

$$\frac{\partial U_{0100}}{\partial T_{11}} = 0\,, \tag{A 20}$$

indicates that there is no energy exchange between the Langmuir circulation and the internal waves over the T_{11} time scale. Consideration of the internal-wave dynamics at $O(k\varepsilon\delta_-)$, however, yields the following non-trivial solvability condition:

$$\frac{\partial U_{0010}}{\partial T_{11}} = -\mathrm{i}\left[\frac{90(R_*^2\gamma F - 60)}{R_*^5\gamma F c}\right] U_{0100}\,U^*_{0001}. \tag{A 21}$$

Thus, the $O(k\varepsilon\delta_-)$ quadratic nonlinear interaction between the stationary Langmuir circulation and the negatively propagating internal wave modulates the $O(\delta_+)$ amplitude of the positively propagating wave.

REFERENCES

Chini, G. P. 1999 Resonant interaction of large-scale Langmuir circulation and thermoclinic internal waves. PhD thesis, Cornell University.

Cox, S. M. 1997 Onset of Langmuir circulation when shear flow and Stokes drift are not parallel. *Fluid Dyn. Res.* **19**, 149–167.

Cox, S. M. & Leibovich, S. 1993 Langmuir circulations in a surface layer bounded by a strong thermocline. *J. Phys. Oceanogr.* **23**, 1330–1345.

Cox, S. M. & Leibovich, S. 1997 Large-scale three-dimensional Langmuir circulation. *Phys. Fluids* **9**, 2851–2863.

Cox, S. M., Leibovich, S., Moroz, I. & Tandon, A. 1992 Nonlinear dynamics in Langmuir circulations with $O(2)$ symmetry. *J. Fluid Mech.* **669**, 669–704.

Craik, A. D. D. 1977 The generation of Langmuir circulations by an instability mechanism. *J. Fluid Mech.* **81**, 209–223.

Craik, A. D. D. & Leibovich, S. 1976 A rational model for Langmuir circulations. *J. Fluid Mech.* **73**, 401–426.

Farmer, D., Vagle, S. & Li, M. 2001 Bubble and temperature fields in Langmuir circulation. In *Fluid Mechanics and the Environment: Dynamical Approaches* (ed. J. L. Lumley). Springer.

Gnanadesikan, A. & Weller, R. 1995 Structure and instability of the Ekman spiral in the presence of surface gravity waves. *J. Phys. Oceanogr.* **25**, 3148–3171.

Huang, N. 1979 On surface drift currents in the ocean. *J. Fluid Mech.* **91**, 191–208.

Leibovich, S. 1977*a* Convective instability of stably stratified water in the ocean. *J. Fluid Mech.* **82**, 561–585.

Leibovich, S. 1977*b* On the evolution of the system of wind drift currents and Langmuir circulations in the ocean. Part 1. Theory and averaged current. *J. Fluid Mech.* **79**, 715–743.

https://doi.org/10.1017/S0022112003006074 Published online by Cambridge University Press

LEIBOVICH, S. 1983 The form and dynamics of Langmuir circulations. *Annu. Rev. Fluid Mech.* **15**, 391–427.

LEIBOVICH, S. 1985 Oscillatory and competing instabilities in a nonlinear model for Langmuir circulations. *Phys. Fluids* **28**, 2050–2061.

LEIBOVICH, S., LELE, S. K. & MOROZ, I. 1989 Nonlinear dynamics in Langmuir circulations and in thermosolutal convection. *J. Fluid Mech.* **198**, 471–511.

LEIBOVICH, S. & TANDON, A. 1993 Three-dimensional Langmuir circulation instability in a stratified layer. *J. Geophys. Res.* **98**, 16 501–16 507.

LELE, S. K. 1985 Some problems in hydrodynamic stability arising in geophysical fluid dynamics. PhD thesis, Cornell University.

LI, M. & GARRETT, C. 1995 Is Langmuir circulation driven by surface waves or surface cooling? *J. Phys. Oceanogr.* **25**, 64–76.

LI, M. & GARRETT, C. 1997 Mixed layer deepening due to Langmuir circulation. *J. Phys. Oceanogr.* **27**, 121–132.

MCWILLIAMS, J. C., SULLIVAN, P. P. & MOENG, C. 1997 Langmuir turbulence in the ocean. *J. Fluid Mech.* **334**, 1–30.

MEI, C. C. 1985 Resonant reflection of surface water waves by periodic sandbars. *J. Fluid Mech.* **152**, 315–335.

OSTROVSKY, L. A., KAZAKOV, V. I., MATUSOV, P. A. & ZABORSKIKH, D. V. 1996 Experimental study of the internal wave damping on small-scale turbulence. *J. Phys. Oceanogr.* **26**, 398–405.

OSTROVSKY, L. A. & ZABORSKIKH, D. V. 1996 Damping of internal gravity waves by small-scale turbulence. *J. Phys. Oceanogr.* **26**, 388–397.

PAVITHRAN, S. & REDEKOPP, L. G. 1994 The coupling of gravity waves and convection: amplitude equations and planform selection. *Stud. Appl. Maths* **93**, 209–250.

PHILLIPS, O. M. 1977 *The Dynamics of the Upper Ocean*, 2nd edn. Cambridge University Press.

SKYLLINGSTAD, E. D. & DENBO, D. W. 1995 An ocean large-eddy simulation of Langmuir circulations and convection in the surface mixed layer. *J. Geophys. Res.* **100**, 8501–8522.

SKYLLINGSTAD, E. D. & DENBO, D. W. 1999 Upper-ocean turbulence during a westerly wind burst: a comparison of large-eddy simulation results and microstructure measurements. *J. Phys. Oceanogr.* **29**, 5–28.

SMITH, J. 1992 Observed growth of Langmuir circulations. *J. Geophys. Res.* **97**, 5651–5664.

SMITH, J. 1998 Evolution of Langmuir circulation during a storm. *J. Geophys. Res.* **103** (C6).

SMITH, J. 2001 Observations and theories of Langmuir circulation: a story of mixing. In *Fluid Mechanics and the Environment: Dynamical Approaches* (ed. J. L. Lumley). Springer.

SMITH, J., PINKEL, R. & WELLER, R. 1987 Velocity fields in the mixed layer during MILDEX. *J. Phys. Oceanogr.* **17**, 425–439.

TANDON, A. & LEIBOVICH, S. 1995 Simulations of three-dimensional Langmuir circulation in water of constant density. *J. Geophys. Res.* **100**, 22 613–22 623.

THORPE, S. A. 1997 Interactions between internal waves and boundary layer vortices. *J. Phys. Oceanogr.* **27**, 62–71.

https://doi.org/10.1017/S0022112003006074 Published online by Cambridge University Press